The study on the structural evolution and the gas sensing properties of the

PECVD-synthesized graphene nanowalls

Jin Chu^a, Yingjia Han^b, Yiming Li^c, Shukai Duan^a, Peter Feng^c, Xiaoyan Peng^{a,c*}

^aCollege of Artificial Intelligent, Southwest University, Chongging, 400715, China

^bCollege of electronic and information engineering, Southwest University, Chongqing,

400715, China

^cDepartment of Physics, University of Puerto Rico, San Juan, 00931, USA

* Author to whom correspondence should be addressed: pengxy2015@swu.edu.cn

Abstract: This research paper reports on studies of the structural evaluation and room

temperature ammonia (NH₃) gas sensing properties of the 3D graphene nanowalls (GNWs).

Large-area porous GNWs as sensing layers were directly prepared by using a plasma

enhanced chemical vapor deposition (PECVD) technique with the H₂/CH₄ gas mixture as a

precursor. The H₂ plasma etching not only contributes to the structural evolution and

thickness of the maze-liked nanowalls, but also plays important roles on the defect sites of the

surface and effective crystalline size of the PECVD-synthesized GNWs.

The comparative studies of sensing performances show the newly fabricated GNWs

sensors were highly responsive and selective to NH₃ gas with low detection limit at room

temperature. Charge transfer has been confirmed as the dominant sensing mechanism for the

GNWs sensors. The excellent sensing performances of the GNWs demonstrate the 3D

assemblies of 2D graphene nanosheet structure with high surface area, large amount of defect

sites and small crystalline sizes are promising candidate for gas sensing applications.

Keywords: Graphene nanowalls; NH₃ sensor; Structural evolution; H₂ plasma

1. Introduction:

Ammonia (NH₃) gas is considered to be toxic when used at high concentration [1], which

will destroy the health of people and even result in the death of human [2]. Thus, an efficient

sensor to detect NH₃ is very necessary for avoiding the dangerous consequences in

environmental monitoring, agricultural and medical applications, etc. The gas sensor with

enhanced performances requires ultrahigh sensitivity, low detection limit and good

reproducibility. Graphene has specific surface area larger than 2600 m² g⁻¹ when exposed to surface molecules [3]. The adsorbed gas molecules can greatly change the carrier density, and consequently strongly influence the electronic properties of graphene [4–5]. What's more, graphene based sensors have low noise-to-signal ratio due to the significant variations in sensor response compared to intrinsic noises including contact influences or thermal switching, etc [6].

Depending on the specific applications, graphene is conventionally synthesized by many different methods, such as: mechanical and chemical graphite exfoliation [7–8], epitaxial growth [9], chemical vapor deposition (CVD) [10], chemically modified graphene [11] and "unzipping" of carbon nanotubes [12]. Graphene nanowalls (GNWs) are vertically standing 2D nanosheet structures possessing rough surface and oriented-edge induced unique characteristics [13]. Compared to single- or few-layer graphene, 3D assemblies of 2D graphene provide more surface area per footprint. GNWs could be a satisfied analytical architecture for different devices for being accessible for efficient adsorption and electron transfer. For example, GNWs and the composites have been utilized in several fields as biosensor [14], energy storage device [15], capacitor [16], lithium-ion battery anode [17], and photodetector [18–20].

In the recent years, numerous efforts have been devoted to theoretical and experimental studies about the graphene-based nanomaterials for adsorption of gas molecules. Seekaew et al. synthesized a new graphene-based electroluminescent device for room temperature (RT) carbon dioxide sensing application [21]. Hong et al. provided a novel NO₂ gas sensor based on the MoS₂/graphene two-dimensional hybrid materials [22]. Duy et al. [23] performed 3D micro-pillar reduced graphene oxide chemical sensors to detect NH₃ gas. Wu et al. [24] fabricated 3D graphene flowers for enhanced gas sensing to detect NO₂ at RT. Cadore et al. [25] demonstrated that the NH₃ sensing characterizes dependent on the distance between the graphene sensitive surface and the substrates. Achary et al. [26] exploited rGO-CuFe₂O₄ composites as a novel NH₃ sensor with detection limit low to 5 ppm. Liu et al. [27] discovered that fluorinated graphene appeared to have an obvious color alter when explored to NH₃, which was observed directly by naked eyes. However, the study on how the hydrogen

(H₂) plasma etching effects on the morphology, crystalline structure as well as sensing performances of GNWs has not been reported.

In this work, we deposited graphene layers onto Si substrates by an effective and catalyst-free plasma enhanced chemical vapor deposition (PECVD) process. Scanning electron microscope (SEM) and transmission electron microscopy (TEM) were utilized to examine the surface morphologies and structures of the samples. Raman spectroscopies were employed to analyze the sp³/sp² Raman bands ratio, crystalline characteristics and X-ray photoelectron spectroscopy (XPS) was used to examine the chemical bonding of the graphene. Furthermore, we exploited the PECVD-synthesized graphene samples to characterize the NH₃ gas sensing properties, such as: response value, selectivity, reproducibility, and stability. In addition, the growth mechanism of the GNWs and the NH₃ detecting mechanism have also been proposed.

2. Experimental details

2.1. Preparation of the graphene GNWs

GNWs were synthesized on the Si substrates by a PECVD system, where methane (CH₄) gas was used as a precursor and the hydrocarbon was easily etched by the H_2 plasma. Prior to deposition, the Si substrates with thickness of 500 μ m were firstly pretreated at surface by H_2 plasma and then used for graphene nanostructures synthesis.

2.1.1 Substrate pretreatment

The undoped Si (100) substrates without oxide layer were cut into 1 $cm \cdot 1$ cm and heated to 700°C in the CVD chamber with the pressure of to 1 Pa. Then, the H₂ gas with 10 standard cubic centimeters per minute (sccm) flow rate was introduced to obtain a pressure of 26 Pa and a radio frequency (RF) power of 60 W was set for 15 min to improve the adhesion between the Si and the subsequent graphene thin films.

2.1.2 Graphene deposition

After pretreatment, the chamber was pumped down to 1 Pa again and the RF power was increased to 200 W. We synchronously introduced CH₄ and H₂ into the PECVD chamber.

The CH₄ gas flow rate was fixed at 6 sccm and the H₂ gas flow rate was adjusted to 0, 4, 6 and 9 sccm, respectively. The substrate temperature remained at 750°C and the deposition duration was 30 min. After deposition, the as-prepared samples were annealed at 700°C with a H₂ flow rate of 15 sccm for 60 min. Then the samples were quickly cooled to RT.

2.2. Characterizations

The morphologic surfaces of the obtained samples—were investigated by SEM. Micro Raman spectroscopies were obtained by using a Jobin-Yvon T64000 Triple-mate system. A radiation of 514.5 nm was emitted from a coherent argon ion laser and a liquid nitrogen cooled charge coupled device was used to obtain the scattered data (HORIBA Group, Japan). The chemical bonds were characterized by XPS with an MgKα X-ray source. The high-resolution transmission electron microscopy (HRTEM) was measured with JEOL JEM-2100. After characterizations, the sputtered Au layers as electrodes were deposited on both sides of the graphene films. Ti thin films were grown in advanced to improve electrical contact and the adhesion between Au electrodes and the GNWs layers.

2.3. Sensing measurements

After characterizations, the samples were transferred into a stainless steel chamber for sensing performance measurements. Dry air was applied as carrying gas and the relative humidity (RH) inside the chamber was kept at 0% RH during the NH₃ sensing characterizations. The concentrations of NH₃ gases were controlled by adjusting the flow rate of dry NH₃ gas and air. All the sensor measurements were performed at RT, 25°C.

3. Results and discussions

3.1. Characterizations of the graphene nanostructures

Fig. 1 shows the surface morphologies of four porous GNWs samples with large interaction surface areas and plenty of edges on the Si substrates and the representative cross-sectional SEM images. The connected small nanowalls structures were synthesized without H_2 assistance, and the thickness of the samples was approximately 3 μ m, as exhibited in Fig. 1 (A). When H_2 was introduced with the flow of 4 sccm, the maze-liked vertical nanowalls with wide wall-to-wall space were formed, and meanwhile the thickness was

significantly decreased to around 1μm, as verified in Fig. 1 (B). Bigger nanosheets and wider wall-to-wall spacing were observed as shown in Fig. 1 (C) when the flow rate of H₂ increased up to 6 sccm. Further increase of the H₂ flow rate to 9 sccm induced identical morphological surface of the GNWs grown at 6 sccm H₂, as exhibited in Fig. 1 (D), which corresponds to equilibrium condition between the graphene growth and etching at a high H₂ flow rate. Need to note here, the thickness of the samples slightly declined to less than 1μm at equilibrium condition, as exhibited by the cross-section images of GNWs-6 and GNWs-9.

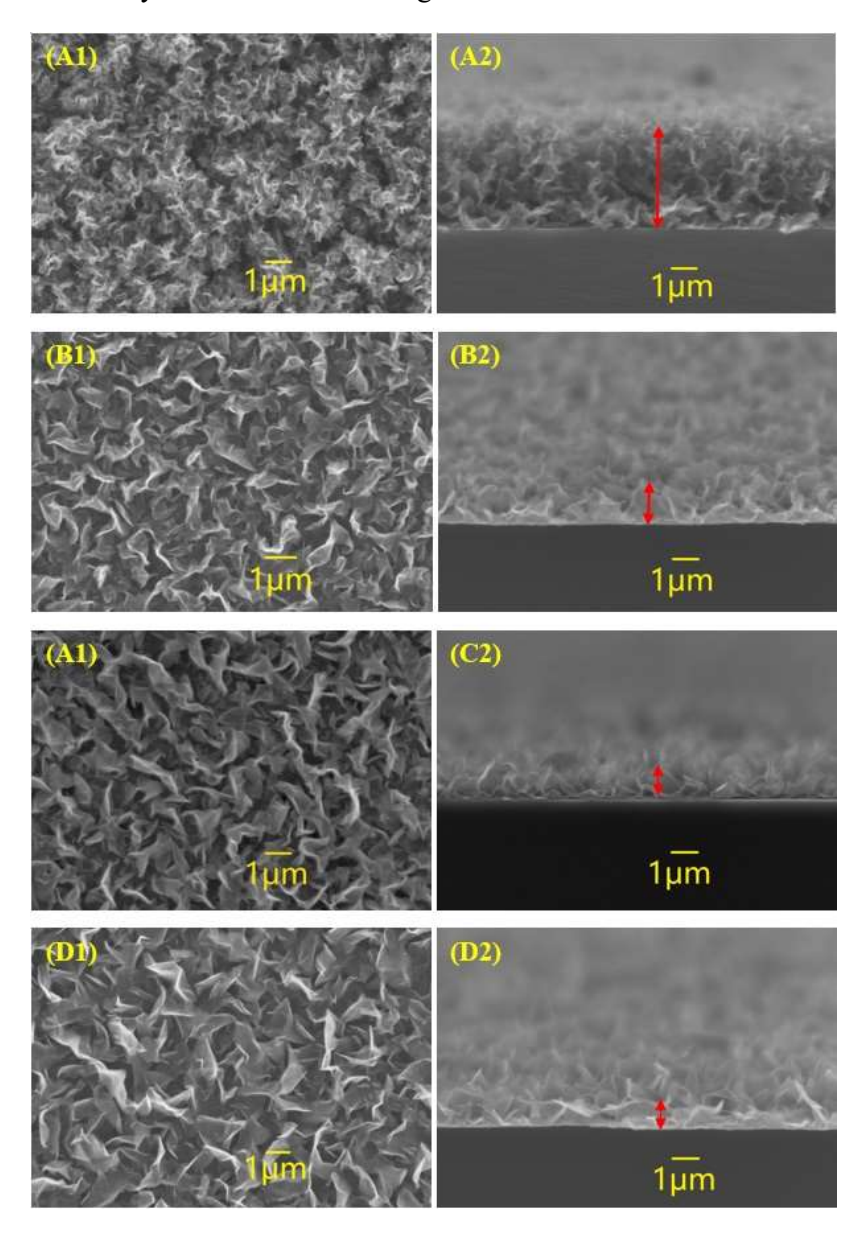
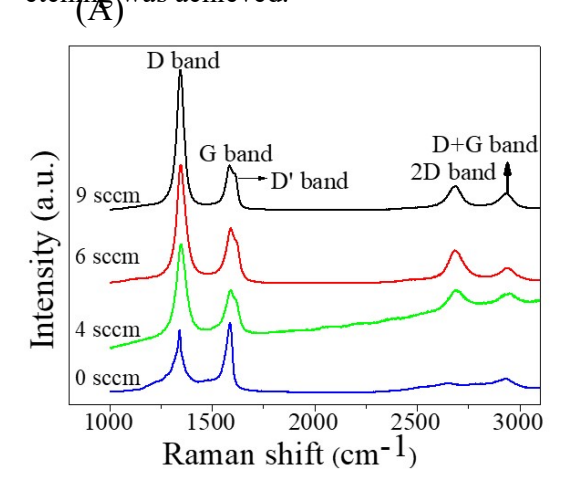


Figure 1 SEM images of the as-prepared GNWs with the H₂ flow rates of (A) 0 sccm, (B) 4 sccm (C) 6 sccm and (D) 9 sccm during the depositions. The samples are labeled as GNWs-0, GNWs-4, GNWs-6, and GNWs-9 respectively in the context.

Compared to the surface morphologies of PECVD-prepared GNWs synthesized by other group without the assistance of H₂[19, 28], the formation of maze-liked GNWs with large scaled vertical nanosheets is strongly dependent on the H₂ plasma contribution, which acts as not only an activator of surface-bound carbon but also an etching reagent that varied the nanowalls distribution and thickness of the graphene. The H₂ plasma could effectively etch the amorphous carbon clusters away from the samples [29]. A two-step model with nucleation and growth can be proposed of GNWs on Si substrate by PECVD. The nuclei were formed on the substrate under the function of the H₂ plasma during the pretreatment process. Dangling bonds associated with nucleation sites were produced and subsequently initiate the growth of small and connected graphene nanowalls [30]. When a small amount of H₂ existed during growth process, the small nucleus could be etched away by H₂ plasma and only the growth of GNWs on the big nucleus survived. Consequently, when the H₂ flow rate was further increased, the size of nanosheets and wall-to-wall space of GNWs grown on bigger nucleus increased. The greatly decreasing of thicknesses of the samples with H₂ injection could be due to the fact that the low growth speed of the GNWs was reduced by H₂ etching process until the equilibrium condition between the graphene growth and the H₂ etching was achieved.



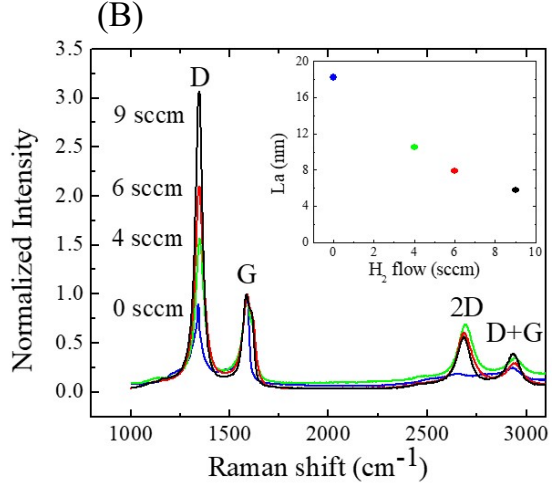


Figure 2 (A) the Raman spectra, and (B) the normalized Raman spectra (respect to the G-peak) with enhanced H_2 partial pressure in the CVD chamber during depositions. The plot of L_a is shown in the inset of (B).

To characterize the etching effect of H₂ plasma on the crystalline structural evolution, the structural attributes of GNWs films were studied by using Raman spectra, as exhibited in Fig.2 (A). The D-peak located at ~1345 cm⁻¹ is associated the structure disorder and higher order electron-phonon scattering, whereas the G band at 1588 cm⁻¹ indicates the graphitized structure, and the accompanied should peak G' observed at 1620 cm⁻¹ is related to graphene edges and finite-size graphite crystals [31–32]. Concomitantly, the presence of 2D peak at 2693 cm⁻¹ represents the layers and crystallinity of graphene [33].

The normalization of Raman spectra (respect to the G-peak) are displayed in Fig.2 (B). The FWHM values of 2D peaks and the $I_{\rm 2D}/I_{\rm G}$ ratios were utilized to analyze the layer stacking characters of the nanowalls [34–35]. It can be observed that the FWHM of 2D peaks and the I_{2D}/I_G ratios for GNWs-0 are quite different from others, while the GNWs grown with H_2 plasma assistant had similar wall thickness, determined by the coincident I_{2D}/I_G ratios of GNWs-4, GNWs-6 and GNWs-9. Furthermore, as shown in Fig. 2 (B), the I_D/I_G ratio of GNWs-0 is close to 0.8, while the D-peak intensity substantially increased with an increase of H₂ partial pressure, proving the presence of graphene edges and defects and a more nanocrystalline structure [30]. The defects and edges which are prevalent for GNWs can be served as adsorption sites and consequently enhance gas adsorption [36]. According to the Tuinstra-Koenig relation [37–38], $A_D/A_G = (560/E_L^4)(1/L_a)$, where A is the net area integrated intensity of the D and G peaks, E_L is the laser energy (electron volts) of the laser and L_a is the correlation length in nanographites, which is usually used to evaluate the effective crystallite size of nanographites. The relationship of the Tuinstra-Koenig correlation length and H_2 partial pressure is exhibited in the inset. It was noted that the L_a calculated by Tuinstra-Koenig relation was synchronously descended with H₂ partial pressure, as shown in inset of Fig. 2, indicating a decreasing in the effective crystallite size [38].

Fig.2 (A) and (B) also exhibit a blue shift of the G-band relative to the unstressed crystalline graphite in Raman spectrum. According to the biaxial strain model, the in-plane compression stress σ of the graphene layer can be evaluated by the following formula [39]:

$$\omega_{\sigma} - \omega_{0} = \alpha \sigma \tag{1}$$

where $\omega_0 = 1580 \ cm^{-1}$ and $\alpha = 7.47 \ cm^{-1}/GPa$ are the G-band location in Raman spectrum and the deformation coefficient of an unstressed crystalline graphene respectively, and ω_{σ} is the position of the G-band of the graphite on Si [39]. A small compression stress of 1.07 GPa of the GNWs samples is calculated by using formula (1), indicating a small stress characteristic of the whole graphene film [40]. What's more, the GNWs are well matched with the Si substrate, which may be of benefit to the long stability of the conductivities of the samples.

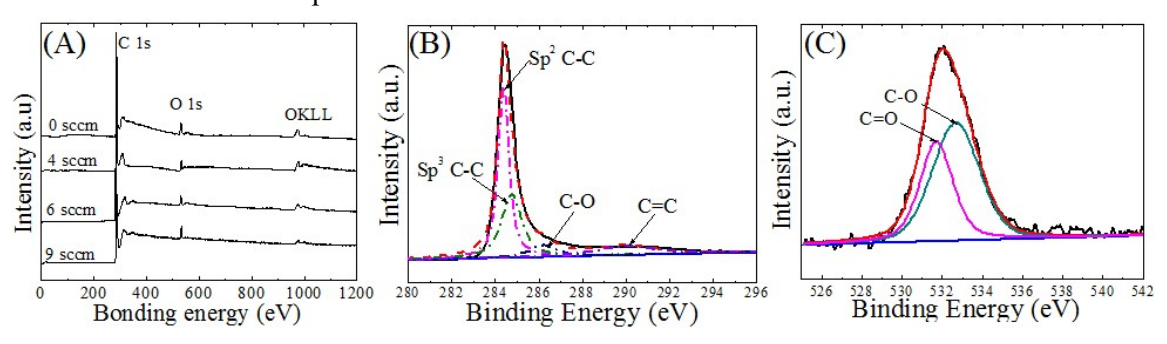


Figure 3 (A) XPS surveys of the samples, and (B) deconvoluted C 1s, (C) O 1s spectra of the GNWs-9 sample.

XPS analyses were performed to verify the chemical contents of the samples, as shown in Fig.3 (A). Two elements C and O were observed in the XPS survey spectra of all the samples, from which the main components of the samples were concluded as C and O, with the calculated C/O ratio of 25.3 of the GNWs-9 sample. The O 1 s and C 1s XPS spectra shown in Fig.3 (B) and (C) indicated two forms of O and C bands: C-O and C=O, which suggests the existence of small amount of oxygen functional groups in GNWs-9 and the defects sites and edges of the GNWs-9 lattice bonded with oxygen. The surface oxygen functional groups can greatly promote the sensing performances of GNWs for acting as adsorption site for testing gas molecules [24].

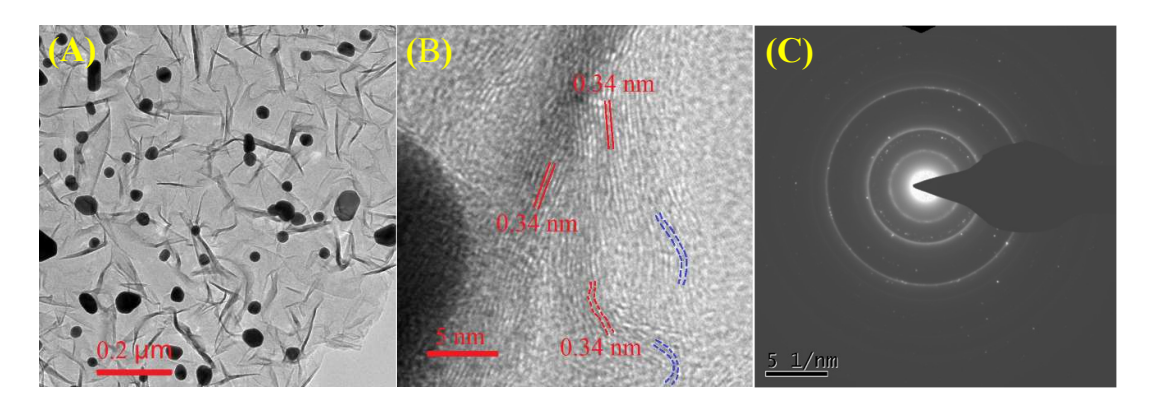


Figure 4 (A) TEM, (B) HRTEM, and (C) SEAD pattern of the GNWs-9 sample.

The structure and morphology of the GNWs-9 was fatherly characterized by HRTEM and the corresponding selected-area electron diffraction (SAED) pattern. The TEM image shown in Fig. 4 (A) displayed the large-scaled and multi-layered graphene with a wrinkled texture. The HRTEM image exhibited the interlayer space about 0.34 nm, which indexed to the (002) plane of a graphitic carbon lattice [41–42], as exhibited in Fig. 4 (B). The blue lines tracing the wrinkled textures of the graphene sheets correspond to the folds and scrolls of the graphene sheets shown in Fig. 4 (A). The ring-liked SEAD pattern with three d spacings (that is, 0.337 nm, 0.217 nm and 0.125 nm), as shown in Fig. 4 (C), indicates a polycrystalline phases of the graphene and stitched grain patches in various orientations [43].

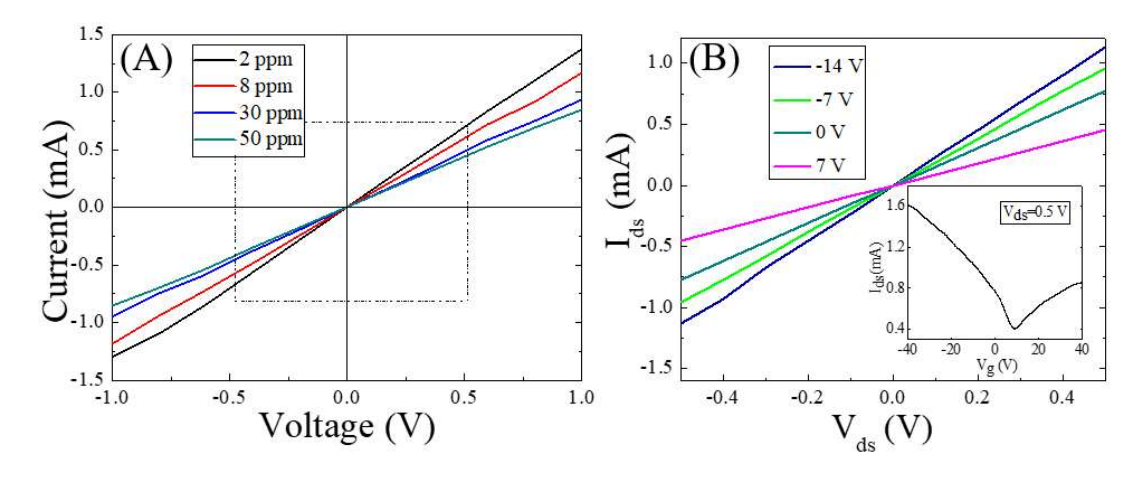


Figure 5 (A) Measured current-voltage (I-V) characteristics of the GNWs-9 sensor at different NH₃ concentration.

(B) I_{ds}-V_{ds} curves of GWNs-based FET with various gate voltages. The inset is the typical transfer characteristic.

Fig. 5 (A) shows the typical I–V curves measured at different static NH₃ concentrations ranging from 2 to 50 ppm for the GNWs-9 sensor at RT. The current-voltage characteristics show strictly linear properties when applied bias voltage was lower than 0.7 V, and the

linearity is slightly degraded at higher voltage, which might be due to the thermal effect. The heat generated by the sample can be expressed as $Q=v^2t/R$, where V is the voltage across the sample and t is the time, as well as R is resistance of the GNWs-9 sensor [11].

The linear I–V curves indicates an ohmic contact between the Au electrodes and the graphene at low voltage. The achievement of the ohmic contact caused by the smooth movements of the electrons within the material [26] and guarantees the accurate evaluation of the interactions between sensors and the target gas [44]. Therefore, a voltage of 0.5 V was applied for the gas sensor characterizations.

In order to determine the semiconductivity of the GNWs, various back gate voltages were applied on the GNWs-9 conductive channel and the corresponding I_{ds}-V_{ds} curves of the GNWs were measured, and shown in Fig. 5 (B). The Field-effect transistor (FET) transfer characteristic is also displayed in the inset of Fig. 5 (B). A drain-source voltage of 0.5 V was applied and the gate voltage was swept from -40 V to 40 V. The Dirac point was at a positive gate voltage of 7 V, indicating a p-type semiconducting behavior of the GNWs-9 [45].

3.2. Sensing properties of the GNWs

After characterizations, the samples were transferred into the sensing characterization system and the sensing performance of the sensors in terms of response, selectivity, reproducibility, and stability were investigated. Response was defined as the percentile resistance change when the sensors are exposed to testing gases as following:

$$Response = \frac{\Delta R}{R_0} \times 100\%$$
 (2)

where $\Delta R = R_g - R_0$, R_0 and R_g are the resistances of the sensor before and after the exposure to testing gas, respectively.

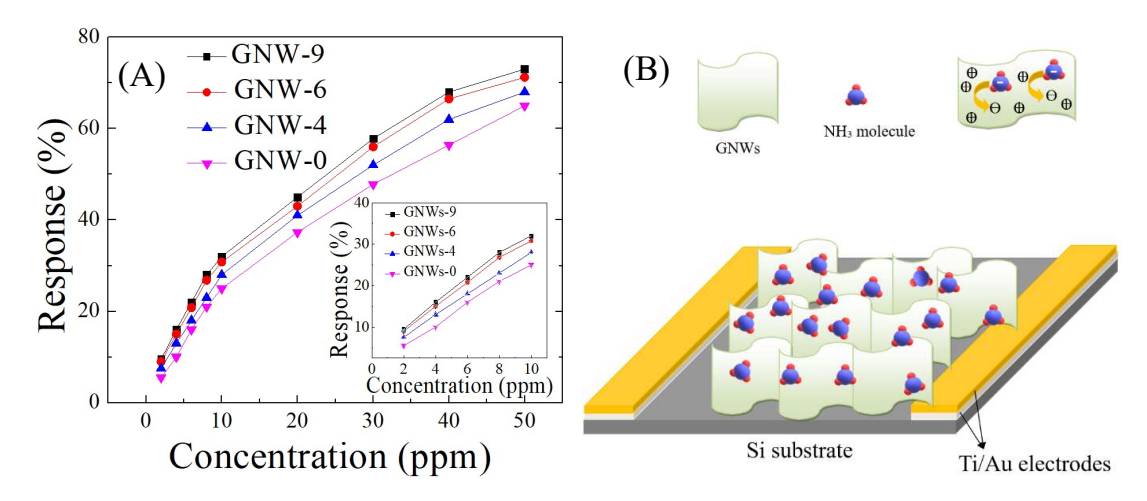


Figure 6 (A) The response comparisons of the samples with respect to the NH₃ concentrations at 25°C and the responses of the samples to different NH₃ concentrations from 2 to 10 ppm are magnified in the inset. (B) The sensing mechanism schematic of the GWNs after NH₃ gas exposure.

The sensing responses of the samples with respect to the NH₃ concentrations at RT are shown in Fig.6 (A). The detection limit was 2 ppm, and the plots of the responses *vs* NH₃ concentrations of all the obtained sensors can be divided into two parts by the linearity. The linear parts of the curves at the range of 2–10 ppm are magnified in the inset of Fig.6 (A).

It can be concluded that the data points of the samples GNWs-6 and GNWs-9 in Fig. 6 (A) fit with Langmuir Isotherm model for gas molecules with equation [46–47]:

$$\frac{\Delta R}{R_0} = \frac{\alpha}{1 + \frac{k_{eq}}{C(ppm)}} \tag{3}$$

Where α is the constant determined by the transport property of sensors, $k_{_{eq}}$ is the gas adsorption equilibrium constant, and for our case, C is the NH₃ gas concentration in ppm. For GNWs-9, the α and $k_{_{eq}}$ are calculated as 124 and 35, respectively.

The response vs gas concentration curves for all the samples can be divided into two ranges as 2–8 ppm and 8–50 ppm. When the gas concentration is lower than 8 ppm, Eq. (3) can be evolved as $\Delta R/R_0 = (\alpha/k_{eq}) \cdot C$, indicating a linear correlation between the sensor response and the concentration of NH₃ gas in ppm. For example, the response vs

concentration curve's slope of sample GNWs-9 is around 3.55 calculated by α/k_{eq} when the concentration is 2–8 ppm, which is accordance to the slope of the curve as shown in the inset.

Charge transfer can be confirmed as the dominant sensing mechanism since the response vs concentration curves fit well with the Langmuir Isotherm for surface absorbed molecules [47]. The relationship between the sensor's transient behaviors and the concentration of the target gases can be understood with the energy bonding site. The gas molecules are adsorbed either on a lower-energy or a higher-energy binding site of graphene [48]. The higher-energy binding sites were occupied by the initially absorbed gas molecules. With the increase of gas concentration, lower-energy adsorption with weak interactions takes place after the exhaustion of the adsorption surface sites [49], the response increasing rate is lower than that at initial period.

A sensing mechanism for the GWNs-9 sensor after NH₃ exposure was proposed, as shown in Fig. 6 (B). The absorbed NH₃ gas molecules with electron-donating ability transfer charge electrons to the p-type graphene and then the number of holes was reduced [8, 50]. As a consequent, the resistance of the graphene based sensor was increased. The excellent sensing performances for the PECVD-synthesized GNWs can be attributed to following four factors: (1) the vertical nanosheet structures makes the graphene highly sensitive to the adsorption of the gas molecules through electron transport [51]; (2) the large amount of defects sites of the samples provides more adsorption spots of the NH₃ gas molecules; (3) the L_a of the nanographites of this work is much less than the reported data [38], implying small crystalline size and a larger surface to volume ratio of the samples in the present work. Therefore, it provides a larger specific surface area and more sensing sites that would greatly enhance the gas molecule adsorptions [52]; (4) the bonding between the NH₃ molecules and the oxygen functional groups facilitate NH₃ adsorptions, resulting in an increase of sensing capability. By comparing the sensing performances of the samples, GNWs-9 appear to have the highest response strength, which can be explained by the largest defect concentration and the smallest crystalline size of GNWs-9 among all the samples. Therefore, we would mainly

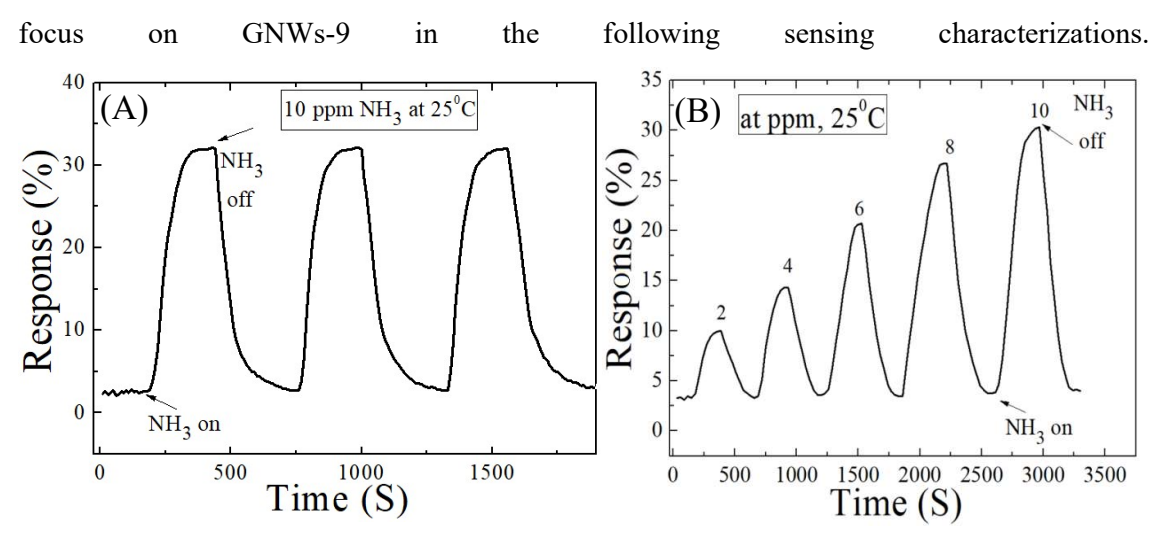


Figure 7 (A) Transient behavior of the GNWs-9 sensor to 10 ppm NH₃ gases, (B) Dynamic response of the GNWs-9 sensor upon exposure to NH₃ gases with concentration increased from 2 to 10 ppm at 25°C.

The GNWs-9 sensor was exposed to 10 ppm NH3 for several cycles to investigate the reproducibility. When the adsorption-desorption behaviors were repeated, the responses of GNWs-9 sensor were recoverable, as exhibited in Fig.7 (A), indicating the fabricated sensor has excellent reproducibility and good stability, which may benefit by the numerous oxygen element of CVD-synthesized GNWs (confirmed by XPS).

The electron transmission was happened between the absorbed NH3 molecules and the oxygen derivatives and consequently the adsorption and desorption behaviors are reversible at RT [45]. The transient response behaviors of the GNWs-9 sensor to different NH₃ concentrations are displayed in Fig. 7 (B). When the NH₃ gas was switched off, the response strength decreased to a stable value. On the contrary, when the sensor was exposed to a certain NH₃ concentration again, the response of the GNWs-9 sensor was enhanced and then recovered to the initial value. One of the advantages of the GNWs based sensor is the aid of extra complicated circuit [53], functionalization treatment [54] or heterostructures [25] is not required during the response and recovery process, which allows room-temperature high qualified and reversible sensing.

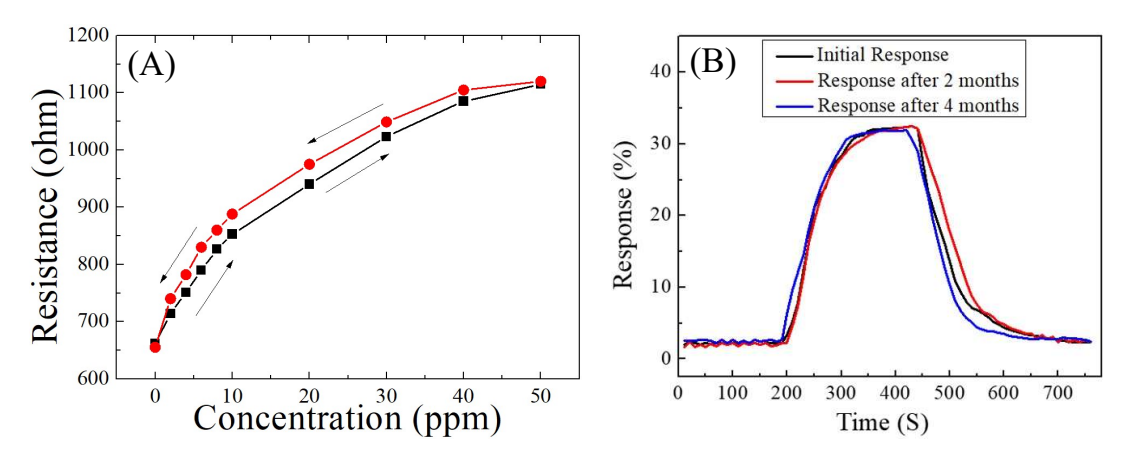


Figure 8 (A) The resistance hysteresis loop of the GNWs-9 sensor against NH₃ concentration arranging from 2 to 50 ppm at 25°C, (B) The long-term stability of the GNWs-9 sensor at 10 ppm NH₃ concentration over a period of several months.

Fig.8 (A) shows the resistance hysteresis characteristic of the GNWs-9 sensor. The electron transfer between the NH₃ molecules and the GNWs-9 increases with enhanced NH₃ molecules concentration, and then consequently leads to the variation of the resistance of the GNWs-9 sensor. The concentration was started from 2 ppm and ended at 50 ppm. Then the concentration was decreased to 2 ppm again. The maximal resistance hysteresis is about 4.53% at 10 ppm for the sensor. The conductivity of the GNWs-9 sensor decreased with NH₃ concentration during the concentration variation of 2–50 ppm. The conductivity changes rapidly when the concentration is lower than 10 ppm and then the variation speed becomes slow when the concentration over 10 ppm. This result is in accordance with the conclusion obtained from Fig.6 (A).

Long-term stability was tested on the GNWs-9 sensing over a 4 months period in order to check the reliability of the sensor. Tests were performed for NH₃ detection at 10 ppm at RT. The results are shown in Fig.8 (B). The initial test followed by subsequent tests performed after 2 months and 4 months. Only slight variations in the NH₃ adsorption and desorption behaviors were observed over time after aging, indicating good stability and durability of the GNWs sensor. The low stress value of the GNWs samples determined by Raman spectroscopy and the low response to the main elements in air ambient may be conductive to the long stability of the sensor.

4. Conclusions

In summary, we have indicated a methodology for synthesis of GNWs by PECVD. The role of H₂ plasma etching on the structural evolution including interim morphologies and crystalline characteristics of GNWs have been studied by changing the H₂ partial pressure during the deposition.

Experimental data clearly indicated that change of the H2 partial pressure during the PECVD deposition could play a very important role on H2 plasma etching that directly determine the structural evolution including interim morphologies and crystalline characteristics of GNWs

It can be concluded that all the PECVD-synthesized 3D GNWs have large interaction surface areas and plenty of edges. However, defects concentration and effective crystalline size, which are estimated through Raman spectroscopy, varied with the H₂ partial pressure. In addition, the existence of the oxygen functional groups revealed by XPS spectra would enhance the adsorption and desorption behaviors of the surface gas molecules at RT.

In addition to the structural evolution study, our work contributes to studying the RT NH₃ gas sensing characteristics of the GNWs. As expected, the GNWs sensors exhibited high response to NH₃ due to large specific surface area and the existence of numerous defects. Especially, the GNWs-9 sensor exhibits high response to NH₃ at low detection limit for the reason of small effective crystalline size and the oxygen functional groups. This study provides a new method in synthesis of 3D nanowall architectures graphene by a simple and economical fashion via PECVD for high-performance gas sensor applications.

Acknowledgement:

The work was supported by National Natural Science Foundation of China (61804127), Fundamental Science and Advanced Technology Research Foundation of Chongqing (cstc2018jcyjAX0261), Fundamental Research Funds for the Central Universities (XDJK2020C040), and NSF-CREST Center for Innovation, Research and Education in Environmental Nanotechnology (CIRE2N) Grant Number HRD-1736093, China Postdoctoral Science Foundation (2017M610582), and Chongqing Postdoctoral Science Foundation

Reference:

- [1] Z. Wu, X. Chen, S. Zhu, Z. Zhou, Y. Yao, W. Quan and B. Liu, Enhanced sensitivity of ammonia sensor using graphene/polyaniline nanocomposite, Sens. Actuators B, 178 (2013) 485–489.
- [2] B. Timmer, W. Olthuis, and A. Van Den Berg, Ammonia sensors and their applications-a review, Sens. Actuators B, 107 (2005) 666–677.
- [3] A. Peigney, Ch. Laurent, E. Flahaut, R.R. Bacsa, A. Rousset, Specific surface area of carbon nanotubes and bundles of carbon nanotubes, carbon. 39 (2001) 507–514.
- [4] X. Du, I. Skachko, A. Barker, and E.Y. Andrei, Approaching ballistic transport in suspended graphene, Nat. Nano., 3 (2008) 491–495.
- [5] K.S. Novoselov, A.K. Geim, S.V. Morozov, D. Jiang, M.I. Katsnelson, I.V. Grigorieva, S.V. Dubonos, and A.A. Firsov, Two-dimensional gas of massless dirac Fermionsin graphene, Nature, 438 (2005) 197–200.
- [6] F. Schedin, A.K. Geim, S.V. Morozov, E.W. Hill, P. Blake, M.I. Katsnelson, and K.S. Novoselov, Detection of individual gas molecules adsorbed on graphene, Nat. Mater., 6 (2007) 652–655.
- [7] E. B. Secor, T. Z. Gao, A. E. Islam, R. Rao, S. G. Wallace, and J. Zhu, et al., Enhanced conductivity, adhesion, and environmental stability of printed graphene inks with nitrocellulose, Chem. Mater., 29 (2017) 2332–2340.
- [8] M. Yi and Z.G. Shen, A review on mechanical exfoliation for the scalable production of graphene, J. Mater. Chem. A, 3 (2015) 11700–11715.
- [9] R. Pearce, T. Iakimov, M. Andersson, L. Hultman, A.L. Spetz, and R. Yakimova, Epitaxially grown graphene based gas sensors for ultrasensitive NO₂ detection, Sens. Actuators B, 155 (2011) 451–455.
- [10] A.N. Obraztov, Chemical vapour deposition: Making graphene on a large scale, Nat. Nanotechnol., 4 (2009) 212–213.

- [11] W. Yuan, A. Liu, L. Huang, C. Li, and G. Shi, High-performance NO₂ sensors based on chemically modified graphene, Adv. Mater., 25 (2013) 766–771.
- [12] D.V. Kosynkin, A.L. Higginbotham, A. Sinitskii, J.R. Lomeda, A. Dimiev, B.K. Price, and J.M. Tour, Longitudinal unzipping of carbon nanotubes to form graphene nanoribbons, Nature, 458 (2009) 872–876.
- [13] X. Song, M. Wang, D. Wei, D. Liu, H. Shi, C. Hu, L. Fang, W. Zhang, and C. Du, Enhanced photoelectrochemical properties of graphene nanowalls-CdS compsite materials, J. Alloys Compd., 651 (2015) 230–236.
- [14] N.G. Shang, P. Papakonstantinou, M. McMullan, M. Chu, A. Stamboulis, A.Potenza, S.S. Dhesi, and H. Marchetto, Catalyst-free efficient growth, orientation and biosensing properties of multilayer graphene nanoflake films with sharp edge planes, Adv. Funct. Mater., 18 (2008) 3506–3514.
- [15] S. Hassan, M. Suzuki, S. Mori, and A. A. El-Moneim, MnO₂/carbon nanowall electrode for future energy storage application: effect of carbon nanowall growth period and MnO₂ mass loading, RSC Adv., 4 (2014) 20479–20488.
- [16] M. Cai, R. A. Outlaw, S. M. Butler, and J. R. Miller, A high density of vertically-oriented graphenes for use in electric double layer capacitors, Carbon, 50 (2012) 5481–5488.
- [17] H. Kim, Z. Wen, K. Yu, O. Mao, and J. Chen, Straightforward fabrication of a highly branched graphene nanosheet array for a Li-ion battery anode, J. Mater. Chem., 22 (2012) 15514–15518.
- [18] X.Z. Liu, Q. Zhou, S. L., H.W. Du, Z.S. Cao, X.Y. Peng, W.L. Feng, J. Shen, and D.P. Wei, Infrared photodetector based on photo-thermionic effect of graphene-nanowalls/silicon heterojunction, ACS Appl. Mater. Inter., 11 (2019) 17663–17669.
- [19] L.F. Li, Y.B. Dong, W.L. Guo, F.S. Qian, F.Z. Xiong, Y.F. Fu,Z.F. Du, C. Xu, and J. Sun, High responsivity photodetectors made of graphene nanowalls grown on Si, Appl. Phys. Lett., 115 (2019) 081101 (5 pages).

- [20] G.L. Lan, J.P. Nong, W.F. Jin, R.R. Zhu, P. Luo, H.B. Jiang and W. Wei, Enhanced UV photoresponse employing 3D graphene nanowalls/SnO₂ nanocomposite film, Surf. Coat. Technol., 359 (2019) 90–96.
- [21] Y. Seekaew, and C. Wongchoosuk, A novel graphene-based electroluminescent gas sensor for carbon dioxide detection, Appl. Surf. Sci., 479 (2019) 525–531
- [22] H.S. Hong, N.H. Phuong, N.T. Huong, N.H. Nam, and N.T. Hue, Highly sensitive and low detection limit of resistive NO₂ gas sensor based on a MoS₂/graphene two-dimensional heterostructures, Appl. Surf. Sci., 492 (2019) 449–454.
- [23] L.T. Duy, D.J. Kim, T.Q. Trung, V.Q. Dang, B.Y. Kim, and H.K. Moon, et al., High performance three-dimensional chemical sensor platform using reduced graphene oxide formed on high aspect-ratio micro-pillars, Adv. Funct. Mater., 25 (2015) 883–890.
- [24] J. Wu, S. Feng, X. Wei, J. Shen, W. Lu, and H. Shi, et al., Facile synthesis of 3D graphene flowers for ultrasensitive and highly reversible gas sensing, Adv. Funct. Mater., 26 (2016) 7462–7469.
- [25] A.R. Cadore, E. Mania, A.B. Alencar, N.P. Rezende, S. Oliveira, K. Watanabe, T. Taniguchi, H. Chacham, L.C. Campos, and R.G. Lacerda, Enhancing the response of NH₃ graphene-sensors by using devices with different graphene-substrate distances, Sens. Actuators B, 266 (2018) 428438–446.
- [26] L.S.K. Achary, A. Kumar, B.Barik, P.S. Nayak, N. Tripathy, J.P. Kar and P. Dash, Reduced graphene oxide-CuFe₂O₄ nanocomposite: A highly sensitive room temperature NH₃ gas sensor, Sens. Actuators B, 272 (2018) 100–109.
- [27] Y. Liu, T.T. Shi, T. Chen, W.J. He, M.M. Chen, and D.W. Cao, The naked-eye NH₃ sensor based on fluorinated graphene, Sens. ActuatorsB, 281 (2019) 789–794.
- [28] D.J. Hsu, Y.W. Chi, K.P. Huang, C.C. Hu, Electrochemical activation of vertically grown graphene nanowalls synthesized by plasma-enhanced chemical vapor deposition for high-voltage supercapacitors, Electrochim. Acta, 300 (2019) 324–332.
- [29] I. Vlassiouk, M. Regmi, and P. Fulvio, et al. Role of hydrogen in chemical vapor deposition growth of large single-crystal graphene, ACS Nano, 5 (2011) 6069–6076.
- [30] M. Hiramatsu, H. Kondo, M. Hori, and J.R. Gong, New Progress on Graphene Research, In Tech: Rijeka, Croatia, 2013; Volume, Chapter 9.

- [31] S. Kurita, A.Yoshimura, H. Kawamoto, T. Uchida, K. Kojima, M. Tachibana, P. Molina-Morales, and H. Nakai, Raman spectra of carbon nanowalls grown by plasma-enhanced chemical vapor deposition, J. Appl. Phys., 97 (2005) 104320 (5 pages).
- [32] A.C. Ferrari, J.C. Meyer, V. Scardaci, C. Casiraghi, M. Lazzeri, F. Mauri, S. Piscanec, D. Jiang, K.S. Novoselov, S. Roth, and A.K. Geim, Raman Spectrum of Graphene and Graphene Layers, Phys. Rev. Lett. 97 (2006) 187401(4 pages).
- [33] J. Shen et al., High-performance schottky heterojunction photodetector with directly grown graphene nanowalls as electrodes, nanoscale, 6 (2017) 6020–6025.
- [34] X. Wang, C.L. Li, Y. Chi, M.X. Piao, J. Chu, H. Zhang, Z.H. Li and W. Wei, Effect of graphene nanowall size on the interfacial strength of carbon fiber reinforced composites, Nanomaterials, 8 (2018) 414 (13 pages).
- [35] A.C. Ferrari, Raman spectroscopy of graphene and graphite: Disorder, electron-phonon coupling, doping and nonadiabatic effects. Solid State Commun., 143 (2007) 47–57.
- [36] A. Salehi-Khojin, D. Estrada, K.Y. Lin, M.H. Bae, F. Xiong, E. Pop, and R.I. Masel, Polycrystalline graphene ribbons as chemiresistors, Adv. Mater., 24 (2012) 53–57.
- [37] M. A. Pimenta, G. Dresselhaus, M. S. Dresselhaus, L. G. Cancado, A. Jorio and R. Saito, Studying disorder in graphite-based systems by Raman spectroscopy, Phys. Chem. Chem. Phys., 9 (2007) 1276–1291.
- [38] R. Narayanan, H. Yamada, M. Karakaya, R. Podila, A. M. Rao, and P. R. Bandaru, Modulation of the electrostatic and quantum capacitances of few layered graphenes through plasma processing, Nano Lett., 15 (2015) 3067–3072.
- [39] Z.H. Ni, W. Chen, X.F. Fan, J.L. Kuo, T. Yu, A.T.S. Wee, and Z.X. Shen, Raman spectroscopy of epitaxial graphene on a SiC substrate, Phys. Rev. B, 77 (2008) 115416 (6 pages).
- [40] S. Novikov, N. Lebedeva, A. Satrapinski, J. Walden, V. Davydov, and A. Lebedev, Graphene based sensor for environmental monitoring of NO₂, Sens. Actuators B, 236 (2016) 1054–1060.
- [41] Y. Shen, and A.C. Lua, A facile method for the large-scale continuous synthesis of graphene sheets using a novel catalyst, Sci. Rep. 3 (2013) 3037 (6 pages).
- [42] W.P. Ouyang, D.R. Zeng, and X. Yu et al., Exploring the active sites of nitrogen-doped

- graphene as catalysts for the oxygen reduction reaction, Int. J. Hydrogen Energ., 39 (2014) 15996–16005.
- [43] F. Gunes, G.H. Han, K.K. Kim, E.S. Kim, S.J. Chae, M.H. Park, H. Jeong, S.C. Lim, and Y.H. Lee, Large-area graphene-based flexible transparent conducting films, NANO: Brief Reports and Reviews, 4 (2009) 83–90.
- [44] H.F. Peng, F. Li, Z.Q. Hua, K.Y., F.X. Yin, and W.J. Yuan, Highly sensitive and selective room-temperature nitrogen dioxide sensors based on porous graphene, Sens. Actuators B, 275 (2018) 78–85.
- [45] S.M. Cui, H.H. Pu, E.C. Mattson, Z.H. Wen, J.B. Chang, Y. Hou, C. J. Hirschmugl, and J.H. Chen, Ultrasensitive Chemical Sensing through Facile Tuning Defects and Functional Groups in Reduced Graphene Oxide, Anal. Chem. 86 (2014) 7516–7522.
- [46] A. Bag, D.B. Moon, K.H. Park, C.Y. Cho, and N.E. Lee, Room-temperature-operated fast and reversible vertical-heterostructure-diode gas sensor composed of reduced graphene oxide and AlGaN/GaN, Sens. Actuators B, 296 (2019) 126684 (10 pages).
- [47] A.N. Abbas, B. Liu, L. Chen, Y. Ma, S. Cong, N. Aroonyadet, M. Köpf, T. Nilges, and C. Zhou, Black phosphorus gas sensors, ACS Nano, 9 (2015) 5618–5624.
- [48] M.G. Chung, D.H. Kim, H.M. Lee, T. Kim, J.H. Choi, D.K. Seo, J.B. Yoo, S.H. Hong, T.J. Kang, and Y.H. Kim, Highly sensitive NO₂ gas sensor based on ozone treated graphene, Sens. Actuators B, 166 (2012) 172–176.
- [49] N.A. Travlou, M. Seredych, E. Rodríguez-Castellón, and T.J. Bandosz, Insight into ammonia sensing on heterogeneous S- and N- co-doped nanoporous carbons, Carbon, 96 (2016) 1014–1021.
- [50] V. Dua, S.P. Surwade, S. Ammu, S.R. Agnihotra, S. Jain, K.E. Roberts, S. Park, R.S. Ruoff, and S.K. Manohar, All-organic vapor sensor using inkjet-printed reduced graphene oxide, Angew. Chem. Int. Ed., 49 (2010) 2154–2157.
- [51] G.H. Lu, L.E. Ocola, and J.H. Chen, Reduced graphene oxide for room-temperature gas sensors, Nanotechnology, 20 (2009) 445502–4455011.
- [52]: X.Y. Peng, M. Sajjad, J.Chu, B.Q. Yang, P.X. Feng, Studies of structural evolution and sensing properties of ZnO nanocrystalline films, Appl. Surf. Sci. 257 (2011) 4795–4800.

- [53] S. M. M. Zanjani, M. H., M. M. Sadeghi, S. Rahimi and D. Akinwande, 3D integrated monolayer graphene—Si CMOS RF gas sensor platform, 2D Mate. Appl. 36 (2017) (9 pages)
- [54] M. Kodu, A. Berholts, T. Kahro, J. Eriksson, R. Yakimova, T. Avarmaa, I. Renge, H. Alles and R. Jaaniso, Graphene-Based Ammonia Sensors Functionalised with Sub-Monolayer V₂O₅: A Comparative Study of Chemical Vapour Deposited and Epitaxial Graphene, Sensors 19 (2019) 951 (17 pages).